

Article

# Movement Control Method of Magnetic Levitation System Using Eccentricity of Non-Contact Position Sensor

Jong Suk Lim and Hyung-Woo Lee \*

Department of Railway Vehicle System Engineering, Korea National University of Transportation, P.O. Box 16106, 157 Cheoldobangmulgwan-ro, Uiwang-si 16106, Gyeonggi-do, Korea; imjong-seok@naver.com

\* Correspondence: krhwlee@ut.ac.kr; Tel.: +82-31-460-0554

**Abstract:** This paper presents a method of utilizing a non-contact position sensor for the tilting and movement control of a rotor in a rotary magnetic levitation motor system. This system has been studied with the aim of having a relatively simple and highly clean alternative application compared to the spin coater used in the photoresist coating process in the semiconductor wafer process. To eliminate system wear and dust problems, a shaft-and-bearing-free magnetic levitation motor system was designed and a minimal non-contact position sensor was placed. An algorithm capable of preventing derailment and precise movement control by applying only control without additional mechanical devices to this magnetic levitation system was proposed. The proposed algorithm was verified through simulations and experiments, and the validity of the algorithm was verified by deriving a precision control result suitable for the movement control command in units of 0.1 mm at 50 rpm rotation drive.

**Keywords:** six degrees of freedom; levitation; movement control; non-contact position sensor; motor system

**Citation:** Lim, J.S.; Lee, H.-W. Movement Control Method of Magnetic Levitation System Using Eccentricity of Non-Contact Position Sensor. *Appl. Sci.* **2021**, *11*, 2396. <https://doi.org/10.3390/app11052396>

Academic Editor: Jeihoon Baek and Andreas Sumper

Received: 9 February 2021

Accepted: 26 February 2021

Published: 8 March 2021

**Publisher's Note:** MDPI stays neutral with regard to jurisdictional claims in published maps and institutional affiliations.



**Copyright:** © 2021 by the authors. Licensee MDPI, Basel, Switzerland. This article is an open access article distributed under the terms and conditions of the Creative Commons Attribution (CC BY) license (<http://creativecommons.org/licenses/by/4.0/>).

## 1. Introduction

Among the semiconductor technologies that are being actively researched recently, semiconductor process technology is one of the core technologies of the semiconductor industry. In semiconductor process technology, research on efficient production strategies of semiconductor manufacturing lines is indispensable and continues to be studied. In recent semiconductor manufacturing lines, most of the equipment is made up of automation equipment, and lots of electrical equipment is used. Among them, the motor is not limited to high power and high efficiency, and studies on environmental aspects such as miniaturization, low vibration, low noise, and heat dissipation characteristics are actively conducted [1].

In general, motors inevitably have problems such as mechanical friction, dust and shaft wear from bearings, which are particularly fatal in semiconductor wafer processing. Particularly, in spin coater machines, a rotating mechanical system used in the photoresist coating process during the wafer process, problems such as dust are a major cause of defective products. Therefore, to solve the defects caused by dust, the problem is solved by installing an additional dust blocking structure. In addition, the wafer photoresist application process requires an additional peripheral positioning system. First, the photoresist spraying nozzle system must have a position control function as it sprays the photoresist at the exact center of the wafer. Secondly, after the photoresist coating process using spin coater rotation, a nozzle position control system EBR (Edge Bead Removal) process system) is indispensable to remove unnecessary portions of the wafer edge.

In the case of general magnetic levitation system research, a tilting system is added to prevent derailment to stably and independently drive the levitation target. Since it is a

system using magnetic levitation, it can solve the problems of mechanical wear and dust, but it has disadvantages as it is complicated and the price increases due to the need for an additional guide (tilting) system [2–4].

Therefore, the magnetic levitation spin coater system was designed to solve the dust problem of the spin coater system, an electric system used in the semiconductor coating process, and to simplify the additional nozzle position control system. Abrasion and dust problems were solved by introducing a non-contact driving method using a magnetic levitation control method. In addition, the spin coater system was simplified by implementing X-Y axis movement control and prevention of derailment was achieved by using only the proposed eccentric movement control technique without using an additional system. The proposed algorithm was simulated using MATLAB/Simulink (R2018a, The MathWorks, Inc., Natick, MA, USA), and a 4 kW magnetic levitation system test model was produced and the experiment was conducted. By verifying the validity of the proposed algorithm based on simulation and test results, it will be possible to greatly improve the problems of dust and system complexity in the semiconductor manufacturing process industry.

## 2. Highly Clean Magnetic Levitation Rotation System for Photoresist Application Process

The spin coating system used in the actual semiconductor coating process is shown in Figure 1. It consists of a position control system of the photoresist spraying nozzle and a wafer rotation device (spin coater) including a spin motor. The spin coater only has a suction function to fix the wafer to the device, and a rotation function to apply the photoresist. Therefore, additional systems such as a peripheral nozzle position control system are needed to be able to spray photoresist from the center of the wafer. In addition, it is composed of a fully enclosed structure to prevent wear on the motor shaft and dust on the bearing.

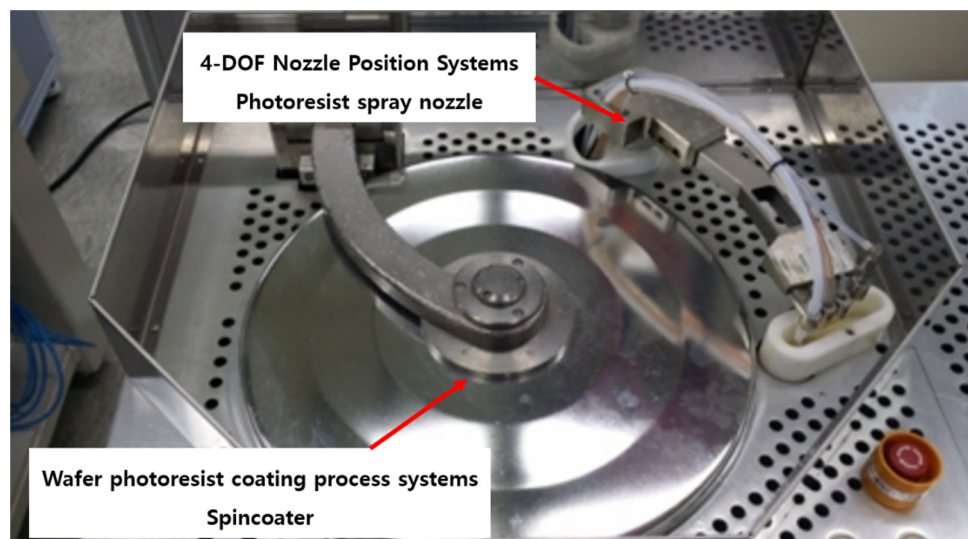


Figure 1. Spin coater used in actual semiconductor wafer process.

Figure 2 depicts a spin coater, a rotating machine system used in the photoresist coating process during the wafer process. As shown in (1) of Figure 2, the problem was solved by installing an additional dust-blocking structure to solve the problem of dust from the motor shaft and bearing. As shown in (2) of Figure 2, the photoresist spray nozzle must also be positioned in the exact center of the wafer, so a nozzle positioning system is required. In addition, after the photoresist coating process using rotation, an additional

process is performed using the nozzle position control system (EBR process system) as shown in (3) of Figure 2 to remove unnecessary portions of the wafer edge, as shown in Figure 3.

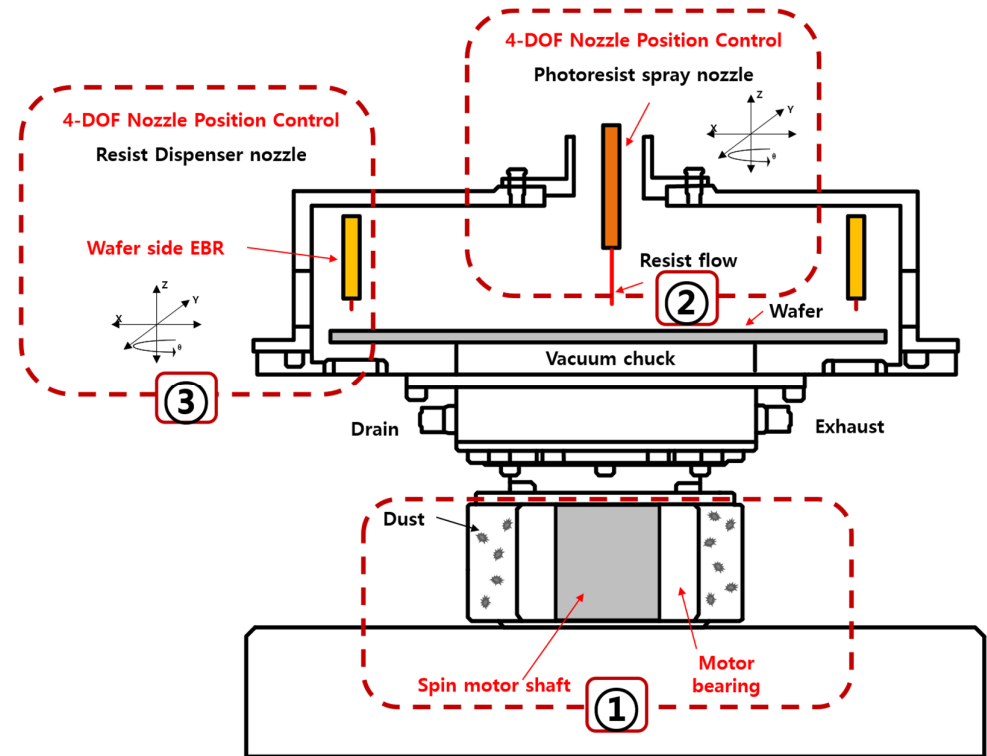
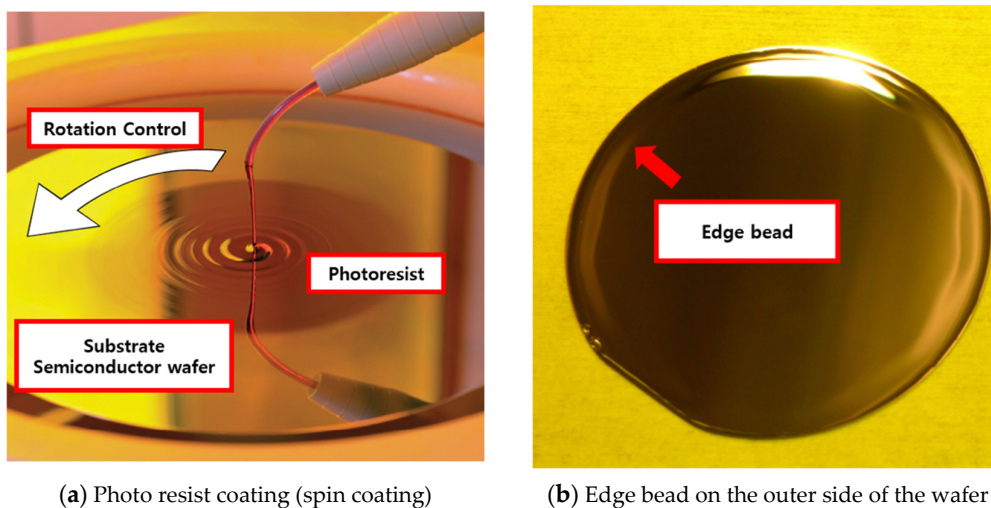


Figure 2. Structure of system used for spin coating (spin coater).



(a) Photo resist coating (spin coating)

(b) Edge bead on the outer side of the wafer

Figure 3. Semiconductor wafer processing and edge bead: (a) photoresist coating (spin coating); (b) edge bead created after the photoresist application process.

In order to solve this problem, a magnetic levitation system is used. This is an application requiring rotational motion by attaching a semiconductor wafer to the top of the system, so the system was configured with an axial permanent magnet motor type as shown in Figure 4. We used a type of surface-attached permanent magnet motor (SPMSM)

designed to place a permanent magnet in the center of the rotor stator coil of the magnetic levitation system.

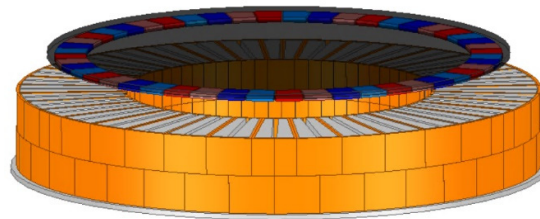


**Figure 4.** Magnetic levitation system composed of the axial motor method using a surface-mounted permanent magnet rotor type.

*2.1. Axial Magnetic Levitation Rotary Motor System without Shaft and Bearing*

In general, vector control, a control technique used to drive a permanent magnet motor, can divide the three-phase current into a magnetic flux current and a torque current having a phase difference of 90° spatially through coordinate transformation. The current in these two components can be controlled independently. As shown in Figure 5, the d-axis current, which is the magnetic flux current, can control the force of the magnetic flux generated  $F_d$  in the vertical direction in the stator. The q-axis current, which is the current for torque, can control the force of the magnetic flux  $F_q$  in the direction of rotation [5–10].

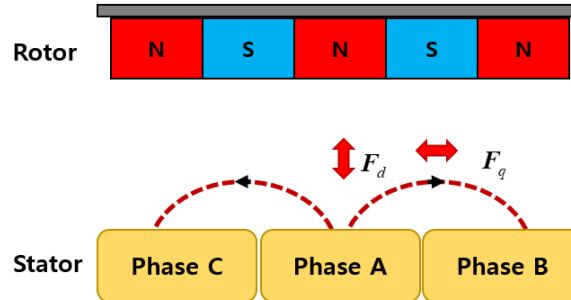


**Figure 5.** Magnetic flux force in vertical and horizontal directions using vector control.

So, vector control in one stator can generate a force that enables two movements. Using these characteristics, the stator of the magnetic levitation system is shown in Figure 6. As shown in Figure 6a, this was divided into four parts: Part A, Part B, Part C, and Part D [11,12]. Each stator consisted of a three-phase stator, for a total of 12 phases. This configuration created a total of eight forces that can be applied to the magnetic levitation rotor. The system was designed to enable stable posture control of the magnetic levitation rotor by using this combination of forces. Also, as shown in Figure 6b, the sensor base was placed in the center of the magnetic levitation system. The non-contact encoder and gap sensor that can measure the rotational position of the rotor are designed by dividing the sensor base into four and placing each [13,14].

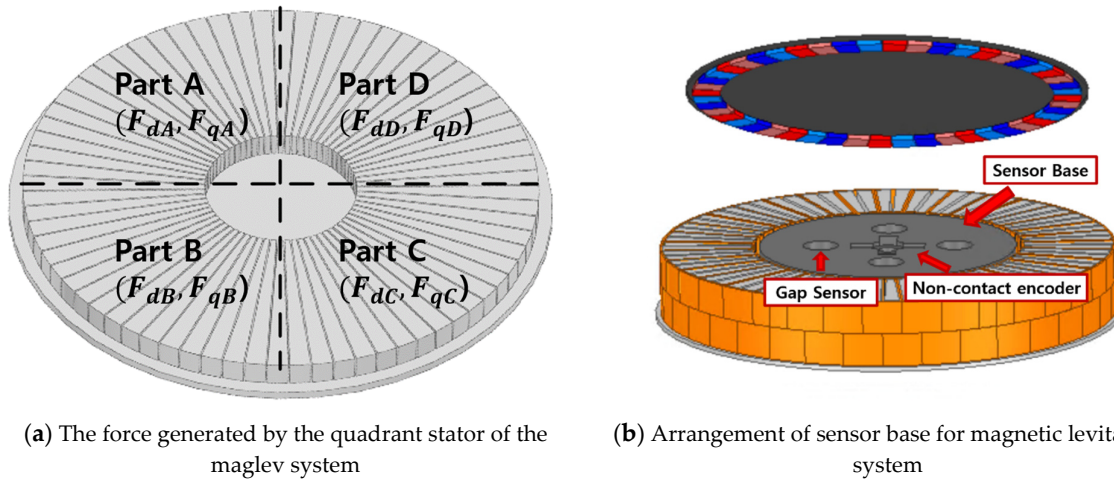


**Figure 6.** Structure of the proposed magnetic levitation system: (a) eight forces generated by the proposed maglev system; (b) arrangement of sensor base with non-contact encoder and gap sensor.

2.2. Reasons for the Need for Derailment Prevention and Movement Control Method

The shaft-and-bearing-free rotary magnetic levitation system can control levitation and rotation by combining a total of eight forces generated by the four-segmented stator. However, when rotational motion of the rotor occurs, a centrifugal force is physically generated as shown in Figure 7. In general, if the rotational force of each section of the same speed is generated, the force of the centrifugal force is balanced in each rotational direction and canceled.

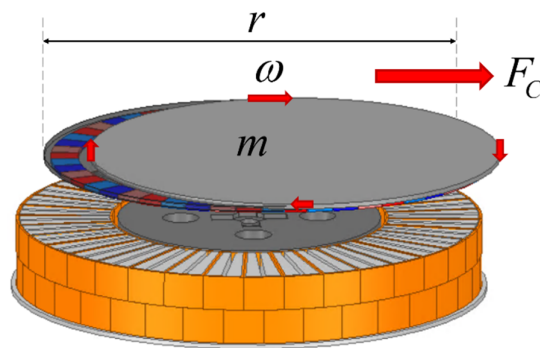


**Figure 7.** Movement of the magnetic levitation system by centrifugal force.

Centrifugal force  $F_C$  is proportional to the mass  $m$  of the rotor and the radius of the rotor  $\frac{r}{2}$  and the rotational speed  $\omega^2$  as shown in Equation (1). If the frictional force is 0 and the rotational speed is different due to a change in inclination or external force, the rotor moves in the direction of centrifugal force [15].

$$F_C = \frac{mr\omega^2}{2} \tag{1}$$

The non-contact encoder senses the scale attached to the center of the rotor to obtain rotation position information, and the sensing range between the scale and the sensor has

limits for vertical and horizontal directions. Therefore, the rotor may be derailed out of the sensing range due to centrifugal force, making it impossible to control.

When a mechanical tilting device is applied to solve this problem, the system becomes large. In addition, in order to simplify the nozzle position control system of the EBR process after the semiconductor wafer photoresist coating process, the X-Y axis movement position control technology of the rotary magnetic levitation system is essential.

### 3. Measurement of Placement Error of Non-Contact Encoder Sensor

Each non-contact encoder sensor arranged on the sensor base acquires position information by sharing one encoder scale attached to the center of the rotor. However, the mechanical placement error and the scale placement error of the non-contact encoder may cause X and Y axis eccentricity, respectively, during rotation control as shown in Figure 8.

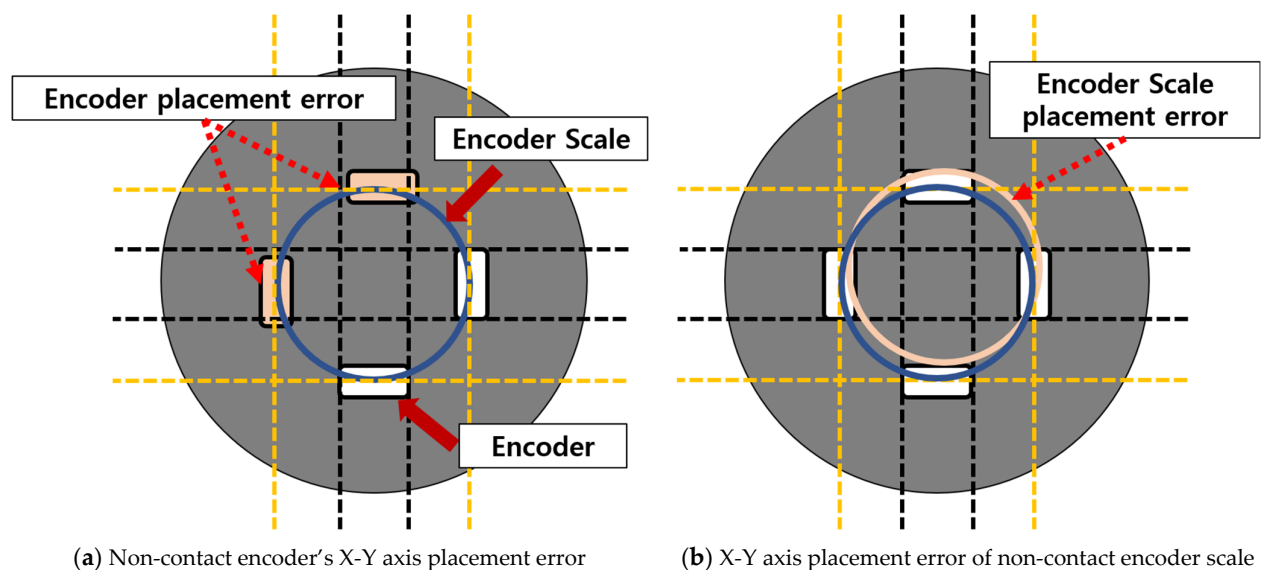


**Figure 8.** Problems caused by attachment error of non-contact encoder: (a) non-contact encoder's X-Y axis placement error (accurate encoder scale placement); (b) encoder scale X-Y axis placement error (accurate non-contact encoder placement).

In Figure 8a, the X-Y axis placement error of the non-contact encoder occurs and the scale is located at the center without any placement error. In the case of Figure 8b, there is no error in the placement of the non-contact encoder, but it represents the occurrence of placement error of the encoder scale. In these two cases, a difference occurs in obtaining information about the rotational position of the same rotor in each stator. Due to the difference in positional information, each stator applies a different current of the rotation command and an eccentricity occurs.

The error distance can be measured by using the error angle that occurs when two non-contact encoders rotate  $180^\circ$ , as shown in Figure 9.

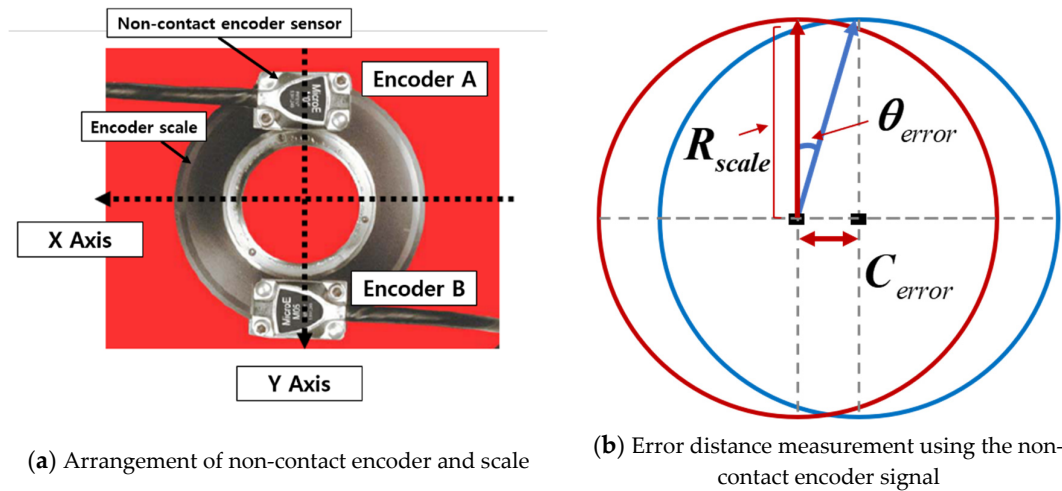


**Figure 9.** Non-contact encoder placement and placement error measurement: (a) non-contact encoder scale and Y-axis encoder arrangement; (b) measurement of distance C caused by placement error of encoder scale and non-contact encoder.

If the error distance of the Y axis is measured as shown in Figure 9a, the encoder scale is sensed by rotating the rotor from the initial positions of non-contact encoders A and B. If there is an arrangement error as shown in Figure 9b, the difference in the rotational position angle of the non-contact encoder B occurs by  $\theta$  at the sensing position of  $180^\circ$  of the non-contact encoder A.

Figure 10 is an enlarged picture of the error distance and error angle in Figure 9b. If the difference between the position information of the non-contact encoder A and B is  $\theta_{error}$  and the radius of the encoder scale is  $R_{scale}$ , the arrangement error distance  $C_{error}$  of the two encoders can be calculated and measured through Equation (2). By additionally measuring the placement error value of the X-axis in this way, all of the placement error values of the X-Y axis can be measured.  $S$  is the arc length when the error range  $\theta_{error}$ .

$$C_{error} = 2R_{scale} \sin \frac{\theta_{error}}{2} \tag{2}$$

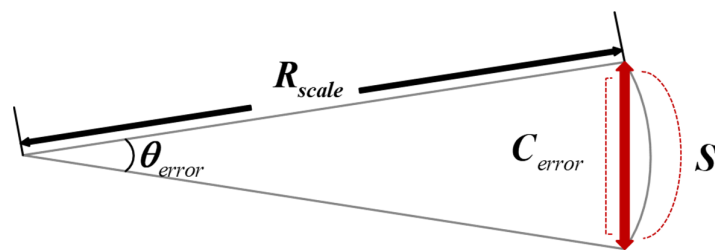


**Figure 10.** Error distance measurement using the difference in position value of two non-contact encoders.

As shown in Figure 8b, the placement error of the encoder scale can also be measured through Equation (2) in the same way. If you acquire position information by setting the error value as a real-time offset value during the initial setup, you can acquire stable rotation position information.

It is assumed that there is no error in the arrangement of the non-contact encoder and encoder scale. If the rotor of the rotary magnetic levitation system is moved by centrifugal force as shown in Figure 11, the same phenomenon as Figure 8b can occur. At this time, the X-Y axis position error value  $C_{translation}$  is the same as the moving distance of the X-Y axis rotor. Therefore, through this method, it is possible to measure the eccentricity of the

magnetic levitation system through the method of measuring the arrangement error of the non-contact encoder.

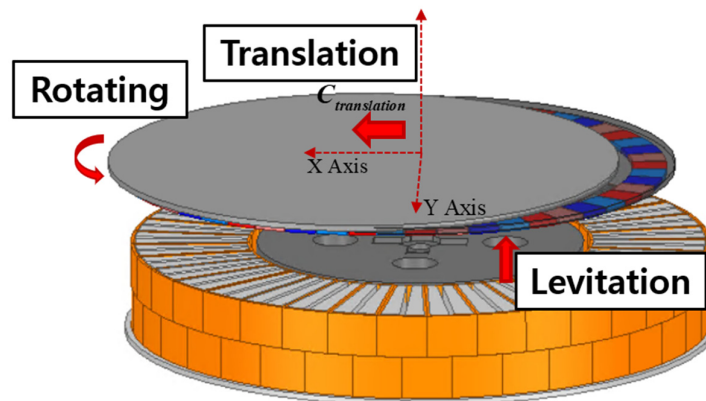


Figure 11. Measurement of travel distance by centrifugal force of magnetic levitation system.

#### 4. Movement Control Algorithm Using Eccentricity

Assuming that the attachment position of the non-contact encoder is correct, the X-Y axis movement distance through movement control has the same meaning as the control that generates eccentricity through control. Therefore, in order to generate the movement control of the magnetic levitation system, it is possible to artificially generate X-Y axis eccentricity by distributing the rotation torque of each stator part.

In the vector control technique of the surface-mounted permanent magnet motor, as described above, the current component can be separated by  $i_d$  and  $i_q$ , and the  $i_q$  component generates a rotational force as a torque equivalent current.

Equation (3) is the equation of the interior permanent magnet motor torque and the current vector. It is composed by using the values for d, q-axis inductance ( $L_d, L_q$ ), number of poles ( $P$ ), and flux linkage ( $\Phi_f$ ) required for torque of a permanent magnet motor [16–19].

$$T = \frac{P}{2} \frac{3}{2} \left[ \Phi_f i_q + (L_d - L_q) i_d i_q \right] \tag{3}$$

However, since the surface-mounted permanent magnet synchronous motor has the feature of non-saliency,  $L_d$  and  $L_q$  can be treated as the same. Therefore, as shown in Equation (4), the torque equation of SPMSM without reluctance torque component can be expressed.

$$T = \frac{P}{2} \frac{3}{2} \Phi_f i_q \quad (L_d = L_q) \tag{4}$$

As shown in Equation (4), the d-axis current  $i_d$  does not contribute to the rotation torque generation.

As shown in Equation (4), the q-axis current command of the four stator parts of the magnetic levitation system is proportional to the rotation torque command.  $F_{rotation}$  refers to the rotational force (torque) of the rotor and is equal to the average of the rotational force of each stator (parts A, B, C, D). Since four stators share one rotor, the current equation for rotation control of the magnetic levitation system can be expressed as Equation

(5).  $I_{rotation}$  is the average rotational current command ( $I_q$ ) of the rotor, and  $I_{qA}, I_{qB}, I_{qC}, I_{qD}$  are the  $i_q$  current command applied to each stator.

$$F_{rotation}^* = \frac{F_{qA} + F_{qB} + F_{qC} + F_{qD}}{4} \approx I_{rotation}^* = \frac{I_{qA} + I_{qB} + I_{qC} + I_{qD}}{4} \quad (5)$$

When a rotational current command is applied as shown in Equation (5), each stator applies a constant  $i_q$  current and the rotor performs a constant rotational motion. The centrifugal force at this time is generated for each rotational direction, as shown in Figure 12 and Equation (6), cancels each other, and converges to zero.

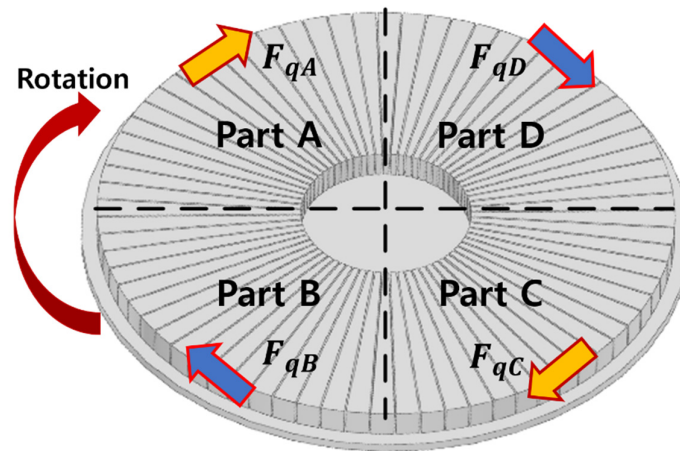


Figure 12. The centrifugal force is canceled by the constant rotational force of each stator.

$$F_C = F_{qA} + F_{qB} + F_{qC} + F_{qD} = 0$$

$$(F_{qA} = -F_{qC}, F_{qB} = -F_{qD}, F_{qC} = -F_{qA}, F_{qD} = -F_{qB}) \quad (6)$$

Therefore, in order to generate eccentricity using centrifugal force as shown in Figure 7, the command of the rotational force in the direction that is offset from each other must be distributed differently. If the rotation direction is set clockwise as shown in Figure 12, the direction of the centrifugal force can be divided by the X-Y axis to be expressed as Equation (7).  $X_{translation}$  is movement in the positive direction of the X axis, and  $F_{XtransC}$  is the centrifugal force in the direction of the X axis.

$$F_{XtransC} = F_{qA} - F_{qC} (X_{translation} > 0)$$

$$F_{YtransC} = F_{qB} - F_{qD} (Y_{translation} > 0) \quad (7)$$

Eccentricity can be caused by generating centrifugal force in the X-Y axis direction using each  $i_q$  current command. It can be seen that the magnitude of the force generated on each axis is proportional to the velocity by the relational equation in Equation (1), and for movement control, a difference in velocity must be placed on each pair of stators. Therefore, the current component of  $i_q$  applied to each stator must have the component for rotation and movement control command, as shown in Equation (8).

$$\begin{aligned}
 i_{qA} &= I_{rotation} + I_{Xtrans} \\
 i_{qB} &= I_{rotation} + I_{Ytrans} \\
 i_{qC} &= I_{rotation} + I_{Xtrans} \\
 i_{qD} &= I_{rotation} + I_{Ytrans}
 \end{aligned}
 \tag{8}$$

For example, in order to include a rotation command that can be changed in real time and an X-axis movement control command in one  $i_q$  current command, the control command is distributed as shown in Equation (9) below. Since each part of the maglev system must maintain the same rotational speed, the same rotational current,  $I_{rotation}ref^*$ , is the input to each  $i_q$  current of the maglev system.

$$\begin{aligned}
 i_{rotation}^* &= I_{rotation}ref^* \\
 i_{Xtranslation}^* &= \frac{I_{Xtrans}ref^*}{2} + \frac{I_{Xtrans}ref^*}{2}
 \end{aligned}
 \tag{9}$$

In the case of the movement control command of  $i_{Xtranslation}$ , it must be distributed to  $i_{qA}$  and  $i_{qC}$  respectively so that the force generated by using the speed difference between Part A and Part C corresponding to the X-axis of the maglev system can be used. Therefore, the rotation and movement control of the rotor can be simultaneously driven by the stator current command of the distributed A part and C part.

$$i_{qA} = I_{rotation}ref^* + \frac{I_{Xtrans}ref^*}{2}
 \tag{10}$$

$$i_{qC} = I_{rotation}ref^* - \frac{I_{Xtrans}ref^*}{2}
 \tag{11}$$

$$i_{qA} + i_{qC} = 2I_{rotation}ref^* + \frac{I_{Xtrans}ref^*}{2} - \frac{I_{Xtrans}ref^*}{2}
 \tag{12}$$

$$i_{qA} + i_{qC} = 2I_{rotation}ref^* = 2i_{rotation}^*
 \tag{13}$$

$$i_{rotation}^* = I_{rotation}ref^*
 \tag{14}$$

$$i_{Xtranslation}^* = i_{qA} - i_{qC} = \frac{I_{Xtrans}ref^*}{2} - \left( -\frac{I_{Xtrans}ref^*}{2} \right)
 \tag{15}$$

$$i_{Xtranslation}^* = I_{Xtrans}ref^*
 \tag{16}$$

As shown in Equations (10) and (11), the  $i_{qA}$ ,  $i_{qC}$  current command of Part A and Part C is arranged by distributing rotation and movement control components. Looking at Equations (12) and (13), the average of the rotation control commands of Part A and Part C becomes  $i_{rotation}ref^*$  as shown in Equation (14). Additionally, it can be confirmed that the X-axis movement control command  $I_{Xtrans}ref^*$  is cleared. If you check the difference between Part A and Part C, as in Equation (15), it can be seen that the sum of the distributed movement control commands is the total movement control command as in Equation (16). If the  $i_{qB}$ ,  $i_{qD}$  command is distributed to Part B and Part D in this way, it can be expressed as a command formula for rotation and Y-axis movement control as shown in Equations (17) and (18) below.

$$i_{qB} = I_{rotation} ref^* + \frac{I_{Ytrans} ref^*}{2} \tag{17}$$

$$i_{qD} = I_{rotation} ref^* - \frac{I_{Ytrans} ref^*}{2} \tag{18}$$

Finally, the rotational position signal uses the calculated  $\theta$  of the non-contact encoder sensor placed on each sensor base. In addition, the position signal for movement control is expressed as Equation (19) using Equation (2) using the difference of  $\theta$  generated when the two non-contact sensors rotate 180 degrees.

$$C_{Xtrans} = 2R_{scale} \sin \frac{\theta_A - \theta_C}{2}, \quad C_{Ytrans} = 2R_{scale} \sin \frac{\theta_B - \theta_D}{2} \tag{19}$$

These two  $i_q$  command components are composed of a system algorithm that can be controlled in real time using a PID double loop as shown in Figure 13.

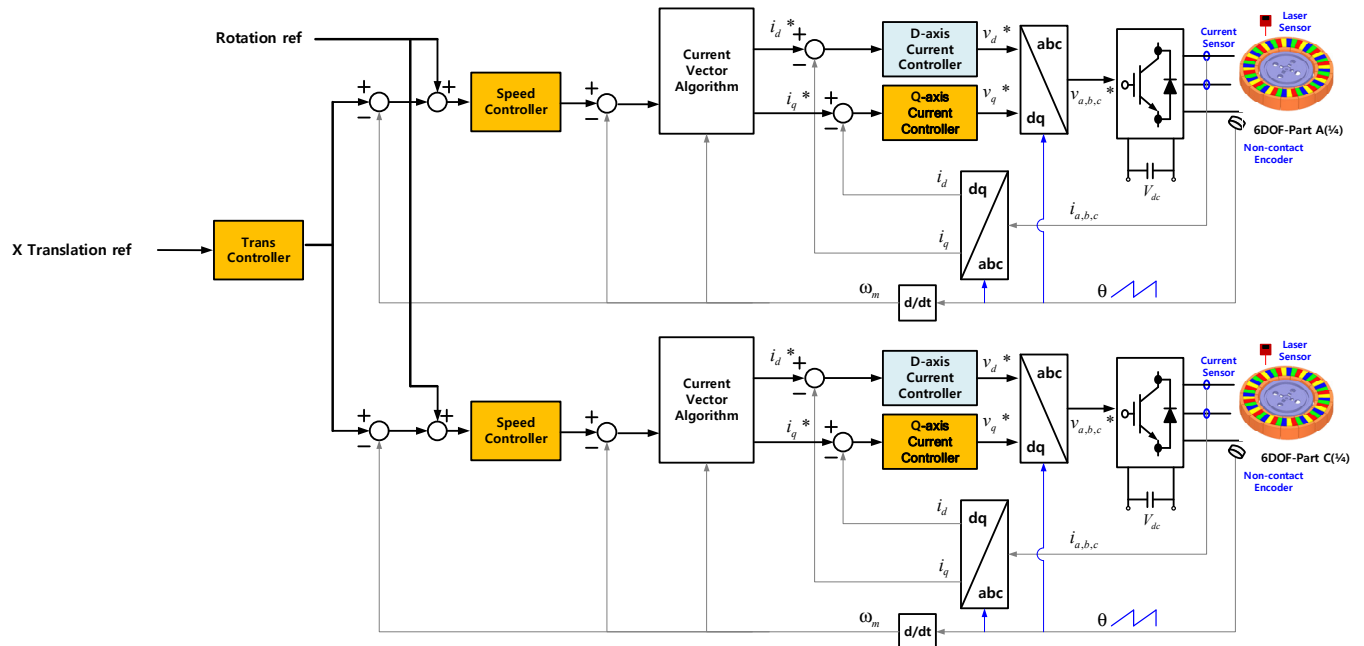


Figure 13. Block diagram of position and velocity control system algorithm using PID double loop.

### 5. Movement Control Algorithm Verification Using Eccentricity

#### 5.1. Movement Control Algorithm Simulation

In order to verify the proposed movement control algorithm using eccentricity, the algorithm and the magnetic levitation system are modeled using MATLAB/Simulink as shown in Figure 14. The magnetic levitation system was configured in the form of 24-pole 72 slots, and the system algorithm was implemented in the configuration of 4CIM in which each controller was connected to four divided stators.

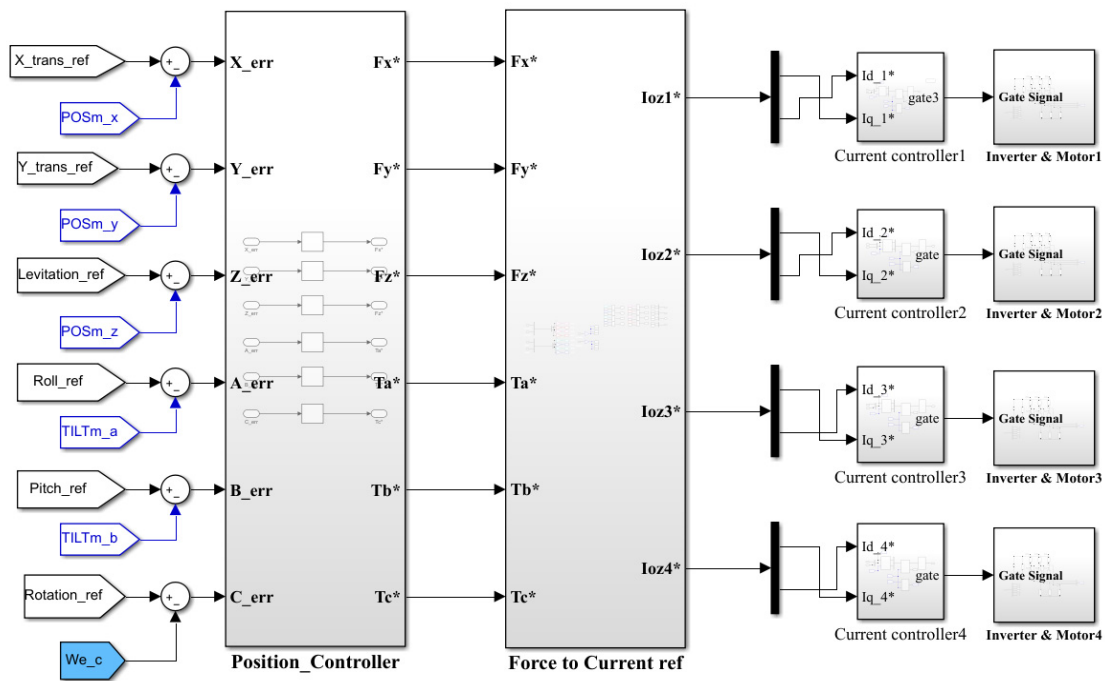
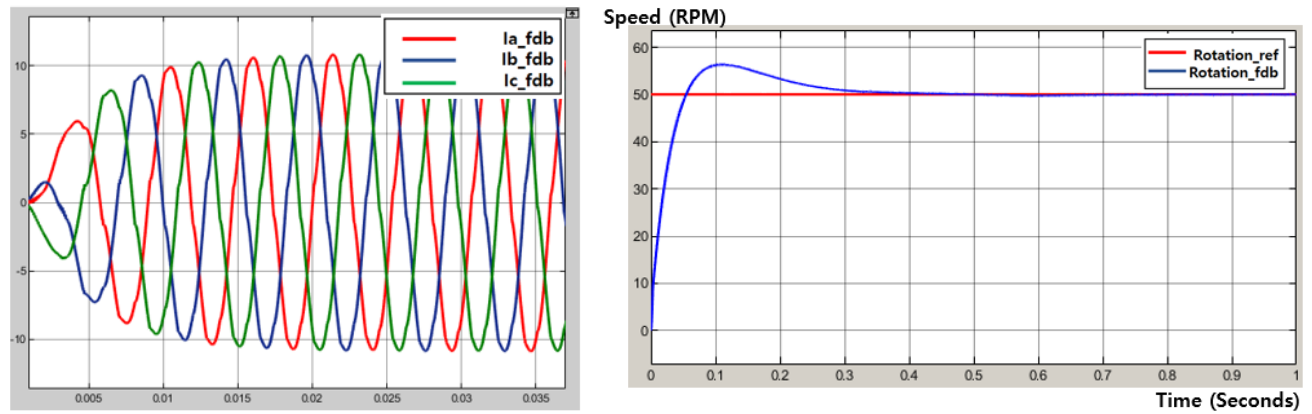


Figure 14. Modeling of maglev system control algorithm using MATLAB/Simulink.

For example, the X-axis movement command ( $X\_trans\_ref$ ) converts the current X-axis position value ( $POSm\_x$ ) and the difference into an error value ( $X\_err$ ) and applies it as the position controller’s command ( $F_x^*$ ). The applied position control command is converted into the current command ( $I_{oz1}^*$ ,  $I_{oz3}^*$ ) of the stator. The converted stator current command is input to the controller through coordinate conversion, output as a voltage signal to the inverter, and drives the magnetic levitation system.

The following figures show the simulation results of the command and output values for rotation and movement control using the magnetic levitation system algorithm modeling.

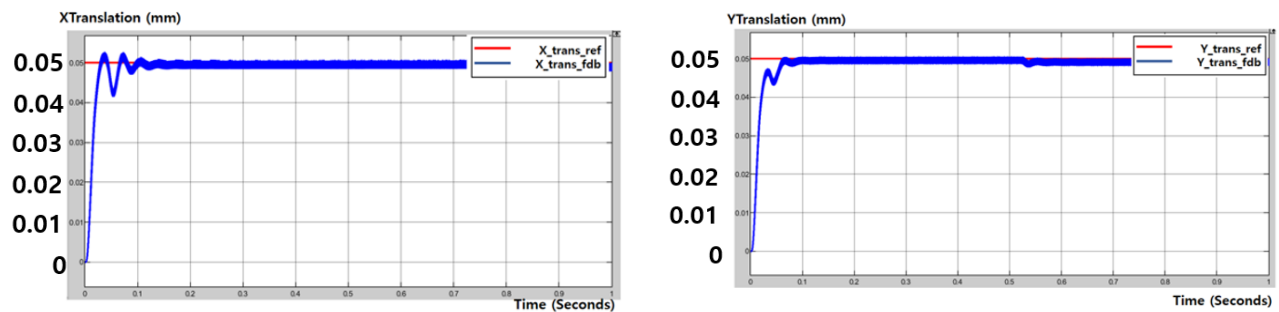
Figure 15a shows the three-phase current of the stator part A generated from the floatation and rotation control of the magnetic levitation system. The weight of the rotor was simulated based on the 1.33 kg of the actual test model. As for the rotation speed command, 50 rpm was applied as shown in Figure 15b, and the levitation command was inputted as 0.2 mm. In addition, 0.05 mm was input for the X-Y axis movement command, and the output characteristics that converge the command values were confirmed as shown in Figure 16.



(a) Three-phase current phase of the Part A stator

(b) Speed output of maglev system

**Figure 15.** Current and speed output using magnetic levitation system algorithm: (a) simulated 3-phase current phase of Part A stator from standstill to 50 rpm operation; (b) simulated command speed 50 rpm and output speed of magnetic levitation system.



(a) X-axis movement control output of magnetic levitation system

(b) Y-axis movement control output of magnetic levitation system

**Figure 16.** X-Y axis movement control output using magnetic levitation system algorithm: (a) X-axis movement control simulation result waveform of magnetic levitation system; (b) Y-axis movement control simulation result waveform of magnetic levitation system.

### 5.2. Experimental Setup and Validation

In the same way as system modeling using MATLAB Simulink, the system is configured as a 24 pole 72 slot 4CIM as shown in Figure 17 so that the system can be controlled by one PC [20].

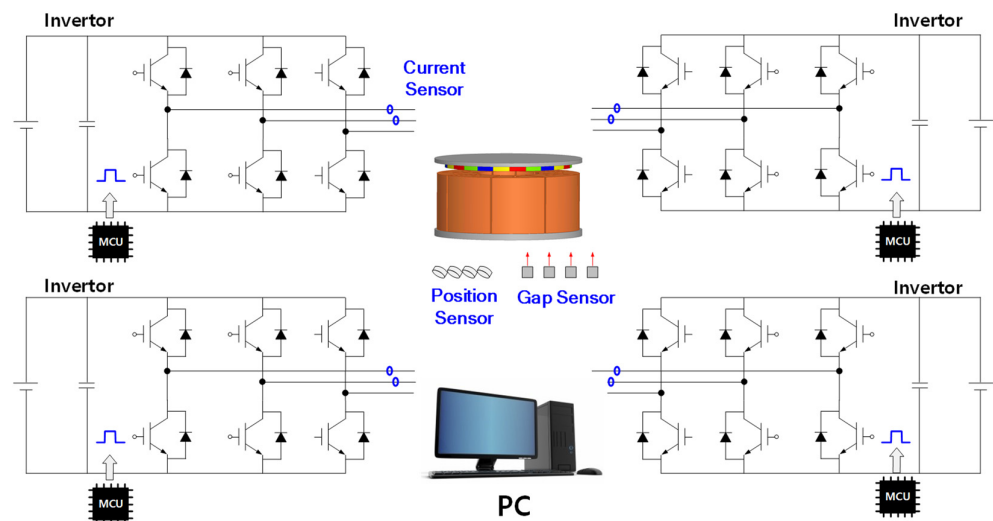


Figure 17. Maglev system consisting of 4 controllers and 1 motor (4CIM).

As shown in Figure 18a, a sensor base is installed in the center of the stator, and a gap sensor and a non-contact encoder sensor are placed. Finally, each inverter and controller were connected to the four divided stators and attached to the system to make an actual magnetic levitation system. Figure 19 shows the final fabricated magnetic levitation system.

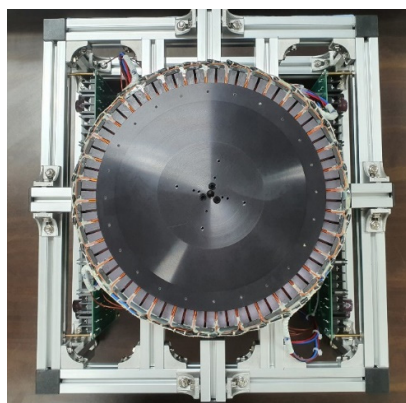


(a) Stator and sensor base of maglev system



(b) Rotor of maglev system

Figure 18. Stator and rotor of magnetic levitation system designed for testing: (a) sensor base with magnetic levitation system stator and non-contact encoder sensor; (b) rotor with non-contact encoder scale of magnetic levitation system.



(a) Top of the test maglev system (b) Side of the test maglev system

**Figure 19.** Manufactured shaft- and bearing-less magnetic levitation system test model: (a) top of the test maglev system; (b) side view of a test maglev system with 4 inverters attached.

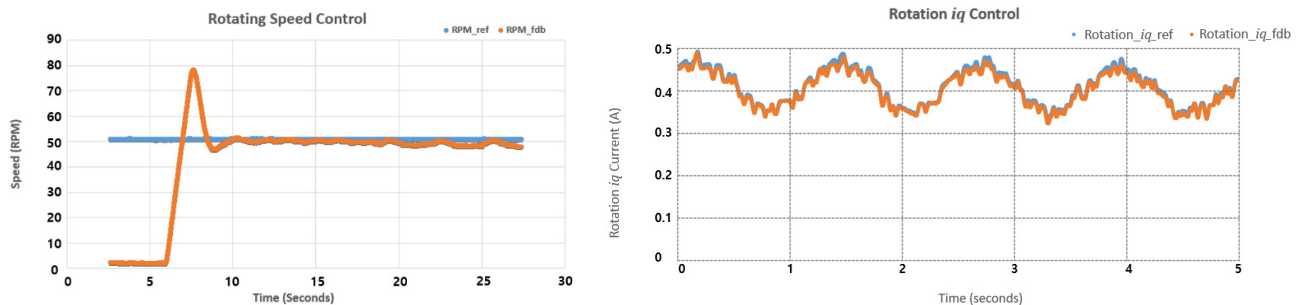
The specifications of the 4 encoders and 4 gap sensors used in the experiment are shown in Table 1. The non-contact encoder sensor used in the experiment is a MicroE Mercury 3000 incremental encoder (MicroE Systems, Bedford, Massachusetts, United States). It is a high-precision position sensor that outputs 8192 pulses per rotation and can be used with high resolution. Additionally, the ODSL9/d26-100-s12 laser sensor (Leuze electronic, Unterstadien, Germany) was used as the gap sensor. It is a laser sensor with a detection distance of 50–100 m and a resolution of 0.01 mm. The sensing height of the non-contact encoder is limited to a maximum of 2.55 mm. In addition, the X-Y axis movement limit has a limit of 0.2 mm in the positive and negative directions. Experiments were conducted to enable precise control within the limits of this sensor specification.

**Table 1.** Specifications of the sensor used in the experiment.

Type	Product name	Resolution
Non-contact encoder	MicroE Mercury 3000	8192(*fold) pulse/rotation
laser sensor	ODSL9/d26-100-s12	0.01 mm <sup>1</sup>

<sup>1</sup> Detection distance 50–100 mm.

Using this experimental equipment, it can be confirmed that the average speed of each part reaches 50 rpm according to the speed command of the magnetic levitation motor as shown in Figure 20, and the  $i_q$  current command is also well converged.



(a) 50 rpm speed control output waveform

(b)  $i_q$  current command and output waveform

**Figure 20.** Rotation control using  $i_q$  current of magnetic levitation system (50 rpm): (a) output waveform of speed control using  $i_q$  current of magnetic levitation system(50 rpm); (b)  $i_q$  current command and output waveform generated during rotation control of magnetic levitation system.

Looking at the output waveforms in Figures 21 and 22, it was confirmed that the movement control using eccentricity was also output consistently according to the 0.1 mm control command.

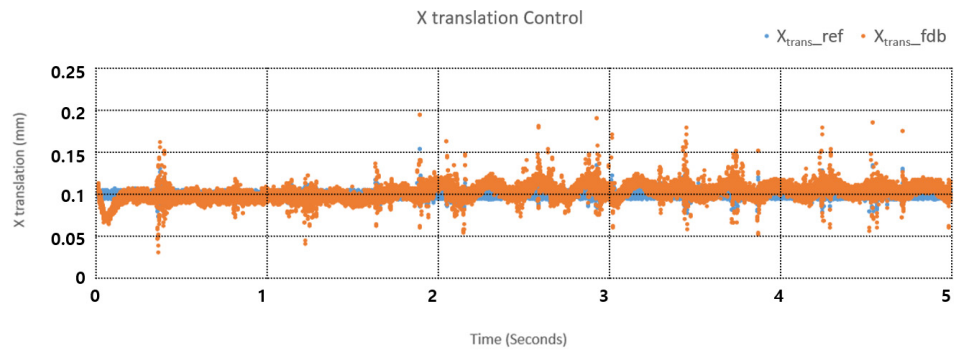


Figure 21. X-axis movement control command and output waveform (0.1 mm command).

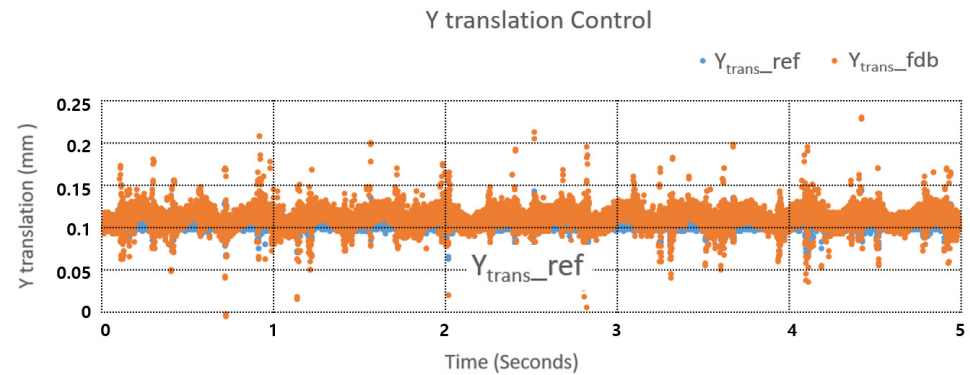


Figure 22. Y-axis movement control command and output waveform (0.1 mm command).

Finally, Figure 23 shows the three-phase current waveform applied to the stator Part A to control the rotation of the 1.33 kg magnetic levitation system rotor used in the test by 0.2 mm and 50 rpm rotation and 0.1 mm X-Y axis movement. It can be seen that the current applied for rotation, floatation, and movement control is approximately 13 A each.

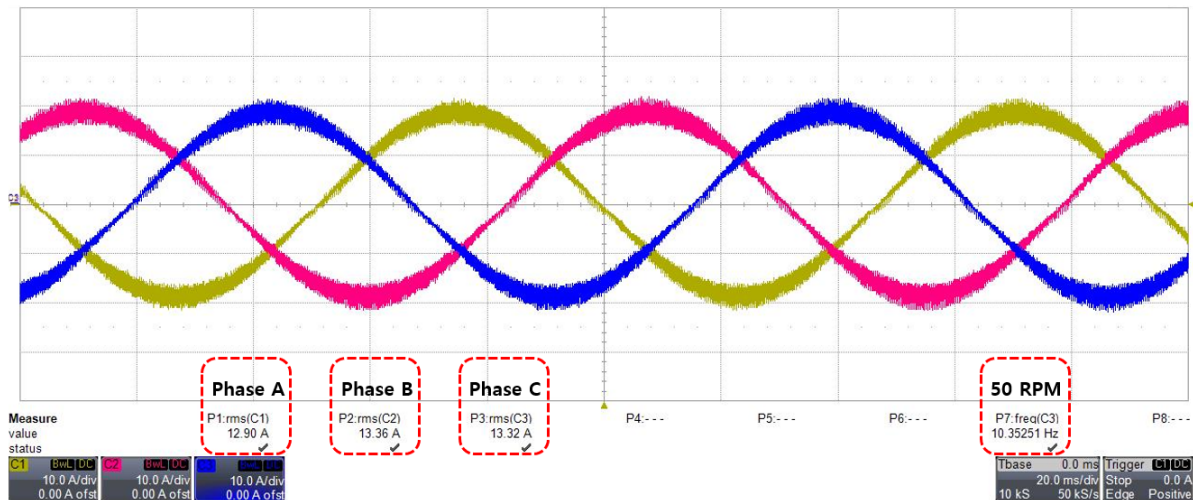


Figure 23. Current waveform of stator Part A using magnetic levitation system algorithm.

### 6. Conclusions

The highly clean magnetic levitation system drive algorithm proposed in this paper can simultaneously perform levitation and rotational motion of a shaft- and bearing-less system as well as motion control using eccentricity.

It is an eco-friendly and simplified system that can take over the role of an additional nozzle position control system by removing the dust generation problem and performing movement control in the semiconductor wafer process, the application field of this study. To eliminate system wear and dust problems, a shaft-and-bearing-free magnetic levitation motor system was designed and a minimal non-contact position sensor was placed. The magnetic levitation system can generate a centrifugal force by creating a condition that can artificially generate the eccentricity of the non-contact sensor by using rotational force. Using this centrifugal force, we proposed an algorithm capable of preventing derailment and precise movement control by applying only control without a separate mechanical device to the magnetic levitation system.

The proposed algorithm was simulated using MATLAB/Simulink. In addition, the validity of the algorithm was verified by deriving a precision control result suitable for the 0.1 mm movement control command at 50 rpm rotation drive through the experiment of the produced test model. Through the proposed movement control algorithm, it is expected that it is possible to drive a precision process system that is eco-friendly, relatively simple, and can have a permanent life in semiconductor processes, thereby securing market competitiveness.

**Author Contributions:** Concept and system design and principle analysis, algorithm development and experiment, J.S.L.; and Manuscript Guide and Correction H.-W.L. All authors have read and agreed to the published version of the manuscript.

**Funding:** This work was supported by the National Research Foundation of Korea (NRF) grant funded by the Korea government (MIST). (No.2020R1F1A1067565).

**Institutional Review Board Statement:** Not applicable.

**Informed Consent Statement:** Not applicable.

**Data Availability Statement:** Not applicable.

**Acknowledgments:** This work was supported by the National Research Foundation of Korea (NRF) grant funded by the Korea government (MIST). (No.2020R1F1A1067565).

**Conflicts of Interest:** The authors declare no conflicts of interest.

## References

1. Teng, Z.; Xiao, J. Surface-Based Detection and 6-DoF Pose Estimation of 3-D Objects in Cluttered Scenes. *IEEE Trans. Robot.* **2016**, *32*, 1347–1361, doi:10.1109/tro.2016.2596799.
2. Jeong, J.-H.; Ha, C.-W.; Lim, J.; Choi, J.-Y. Analysis and Control of the Electromagnetic Coupling Effect of the Levitation and Guidance Systems for a Semi-High-Speed MAGLEV Using a Magnetic Equivalent Circuit. *IEEE Trans. Magn.* **2015**, *52*, 1–4, doi:10.1109/tmag.2015.2506681.
3. Cho, H.-W.; Yu, J.-S.; Jang, S.-M.; Kim, C.-H.; Lee, J.-M.; Han, H.-S. Equivalent Magnetic Circuit Based Levitation Force Computation of Controlled Permanent Magnet Levitation System. *IEEE Trans. Magn.* **2012**, *48*, 4038–4041, doi:10.1109/tmag.2012.2198800.
4. Lim, J.; Jeong, J.-H.; Kim, C.-H.; Ha, C.-W.; Park, D.-Y. Analysis and Experimental Evaluation of Normal Force of Linear Induction Motor for Maglev Vehicle. *IEEE Trans. Magn.* **2017**, *53*, 1–4, doi:10.1109/tmag.2017.2699694.
5. Ko, W.; Ham, C. A Novel Approach to Analyze the Transient Dynamics of an Electrodynamic Suspension Maglev. *IEEE Trans. Magn.* **2007**, *43*, 2603–2605, doi:10.1109/TMAG.2007.893638.
6. Sun, L.; Zhao, K.; Kou, B. An Electromagnetic Launcher with Magnetic Levitation Realized Based on Vector Control. *IEEE Trans. Magn.* **2009**, *45*, 467–470, doi:10.1109/TMAG.2008.2008980.
7. Hwang, S.-H.; Kim, J.-M.; Bang, D.-J.; Kim, J.-W.; Koo, D.-H.; Kang, D.-H. Control of independent multi-phase transverse flux linear synchronous motor based on magnetic levitation. *2014 IEEE Applied Power Electronics Conference and Exposition - APEC 2014* **2014**, 2488–2491, doi:10.1109/apec.2014.6803653.
8. Kobayashi, S.; Ooshima, M.; Uddin, M.N. A Radial Position Control Method of Bearingless Motor Based on d - Q -Axis Current Control. *IEEE Trans. Ind. Appl.* **2013**, *49*, 1827–1835, doi:10.1109/tia.2013.2257972.
9. Lee, H.-I.; Yoo, S.-Y.; Noh, M.D. Toroidally-Wound Self-Bearing BLDC Motor with Lorentz Force. *IEEE Trans. Magn.* **2010**, *46*, 2148–2151, doi:10.1109/tmag.2010.2043065.
10. Cao, J.; Zhu, Y.; Yin, W.; Xu, W. Electromagnetic Forces Acting on the Planar Armature of a Core-Type Synchronous Permanent-Magnet Planar Motor. *IEEE Trans. Magn.* **2009**, *45*, 3145–3150, doi:10.1109/TMAG.2009.2023365.

11. Park, Y. Design and implementation of an electromagnetic levitation system for active magnetic bearing wheels. *IET Control. Theory Appl.* **2014**, *8*, 139–148, doi:10.1049/iet-cta.2013.0450.
12. Ribani, P.; Urbano, N. Study on figure-eight-shaped coil electrodynamic suspension magnetic levitation systems without cross-connection. *IEEE Trans. Magn.* **2000**, *36*, 358–365, doi:10.1109/20.822547.
13. Kim, Y.-K.; Jang, I.G.; Kim, Y.; Kim, K.-S.; Kim, S. Structural Optimization of a Novel 6-DOF Pose Sensor System for Enhancing Noise Robustness at a Long Distance. *IEEE Trans. Ind. Electron.* **2014**, *61*, 5622–5631, doi:10.1109/tie.2013.2297307.
14. Kim, Y.-K.; Kim, K.-S.; Kim, S. A Portable and Remote 6-DOF Pose Sensor System with a Long Measurement Range Based on 1-D Laser Sensors. *IEEE Trans. Ind. Electron.* **2015**, *62*, 5722–5729, doi:10.1109/tie.2015.2410261.
15. Pan, Q.; Huang, F.; Chen, J.; He, L.G.; Li, W.; Feng, Z. High-Speed Low-Friction Piezoelectric Motors Based On Centrifugal Force. *IEEE Trans. Ind. Electron.* **2017**, *64*, 2158–2167, doi:10.1109/tie.2016.2623578.
16. Lee, K.-W.; Kim, S.-I. Dynamic Performance Improvement of a Current Offset Error Compensator in Current Vector-Controlled SPMSM Drives. *IEEE Trans. Ind. Electron.* **2019**, *66*, 6727–6736, doi:10.1109/tie.2018.2877162.
17. Wang, C.-C.; Yao, Y.-D.; Liang, K.-Y.; Huang, C.-C.; Chang, Y.-C.; Lowther, D.A. Axial Vibration Study of a Mobile Fan Motor. *IEEE Trans. Magn.* **2010**, *46*, 1397–1400, doi:10.1109/tmag.2010.2042143.
18. Arakawa, T.; Takemoto, M.; Ogasawara, S.; Inoue, K.; Ozaki, O.; Hojo, H.; Mitani, H. Examination of an Interior Permanent Magnet Type Axial Gap Motor for the Hybrid Electric Vehicle. *IEEE Trans. Magn.* **2011**, *47*, 3602–3605, doi:10.1109/TMAG.2011.2150206.
19. Won, S.H.; Choi, J.; Lee, J. Axial-Gap Type Permanent Magnet Motor Modeling for Transient Analysis. *IEEE Trans. Magn.* **2008**, *44*, 4085–4088, doi:10.1109/TMAG.2008.2002485.
20. Chen, L.; Hu, J.; Zhu, Y.; Du, S.; Chai, Y. A 6-DOF Measurement Solution for Permanent Magnet Synchronous Planar Motors Based on Motion Continuity Principle. *IEEE Trans. Instrum. Meas.* **2016**, *65*, 643–655, doi:10.1109/tim.2015.2509218.